PROCEEDINGS OF SCIENCE

Updated studies of radio propagation through polar firn using paraPropPython

Contribution to ICRC 2023

Alexander Kyriacou[a,*] **on behalf of the Radar Echo Telescope collaboration**

[a] *University of Kansas,*
Lawrence, KS 66045, USA

E-mail: akyriacou@ku.edu

Ultra high energy neutrinos can be detected by measurement of radio emission, produced either from Askaryan emission, or via reflection of an in-ice radar transmission off the neutrino's ionization trail. Accurate reconstruction of the properties depend on accurately modeling radio propagation through the firn layer, the transition between fresh snow and glacial ice, where the refractive index is inhomogeneous over depth and range.

The paraPropPython code uses the parabolic equation (PE) simulation method for improved modeling of RF transmission in polar firn. PE methods permit simulation of arbitrary RF waveforms through data-defined depth and range dependent refractive index profiles on a scale of several kilometres, accounting for features such as surface roughness, crevasses and refrozen-ice layers, and can also model back-scatter off of in-ice anomalies. This work aims to examine the effects of ice inhomogeneities on signal properties using the parabolic wave equation (PE) method of simulation radio propagation, using the upper firn layer of the Greenland ice sheet at the Summit station as an example. We also present improvements and updates to paraPropPython, and show an inversion method to reconstruct refractive index profiles from ice-penetrating radar data.

38th International Cosmic Ray Conference (ICRC2023)
26 July - 3 August, 2023
Nagoya, Japan

*Speaker

PoS(ICRC2023)1073

1. Introduction

Ultra-high energy neutrinos (UHENs) with energies E_ν between $1\,\text{PeV} < E_\nu < 100\,\text{EeV}$ are a window to understanding the high energy universe and the sources of ultra-high energy cosmic rays. Detecting UHENs requires the instrumentation of substantially larger volumes than are feasible with Cherenkov based detectors such as IceCube[1]. Radio waves have an attenuation lengths L_α in polar ice $L_\alpha \sim O(\text{km})$, an order of magnitude (or more) greater than that of optical light, allowing much larger volumes to be instrumented. One approach is to search for UHEN-induced coherent radio emission generated through the *Askaryan effect*[2]. Alternatively, neutrino-(or cosmic ray) induced cascades may be detected by measuring the reflection of radar emission off of the ionization trail left in the UHEN's wake[3], termed the *radar echo* method. The testing of the latter method is the goal of the Radar Echo Telescope for Cosmic Rays[4], currently in operation at Summit station on the Greenlandic ice-sheet.

In both cases, accurate reconstruction of the primary's properties (energy, arrival direction etc.) is dependent on accurately modelling the radio propagation through the ice environment. Current radio neutrino reconstruction analyses have mostly relied on the ray-tracing approximation[5–8], taking the infinite frequency limit and neglecting the wave-like properties of the emission. Finite Difference Time Domain (FDTD) methods provide a full solution of Maxwell's equations, but are too computationally expensive to simulate the required geometries[5]. These studies have also relied on analytical fits to real-world refractive index n profiles [5–8], which presuppose a continuous density gradient and neglect inhomogenities that exist in real world ice caps. These inhomogeneities can modify the measured RF signal amplitude throughout the ice geometry as well as the propagation time and phase[9]. Large density fluctuations, caused by surface melting and refreezing can induce in-ice reflections that can complicate reconstruction analyses.

2. Radio propagation simulations with PEs

The parabolic equation (PE) simulation method is derived from an approximation of the wave solution of Maxwell's equations with the assumption of time-dependence of a scalar field ψ governed by $e^{i\omega t}$,

$$\nabla^2\psi + k_0^2 n^2 \psi = 0, \tag{1}$$

given the vacuum wave vector k_0 and some refractive profile n. Assuming cylindrical symmetry, it obtains a solution for a vertically polarized electric field $\hat{\mathbf{E}}(x, z, \phi) = E_z(x, z)$ (with x being the radial distance coordinate) propagating forwards and backwards in the 'paraxial' direction, which is perpendicular to the field polarization[10]. The approximation allows PE to be solved in a spatial grid in iterations over the range direction x, beginning at the at the origin, and given a solution of the depth dependent field at $x = 0$,

$$u(x + \Delta x) = \exp\left(ik_0(1 - Q)\right) \cdot u(x). \tag{2}$$

Where $u(x, z)$ is the 'reduced field' $u(x, z) = E(x, z)e^{ik_0 x}/\sqrt{x}$. The pseudo-differential operator Q allows the for the equation to be factorized in such a way to permit a step-wise solution. For in-ice propagation, this method uses a second order expansion of the operator[10]:

$$Q = \sqrt{\partial_z^2 + n^2} \approx Q_{\text{ice}} = \sqrt{1 + \partial_z^2/k_z^2} + n\sqrt{1 + (1/n_0)^2} - \sqrt{1 + (n/n_0)^2}, \tag{3}$$

Where $n = n(x, z)$ is a function of depth and range and n_0 is a reference value at some arbitrary depth and range. PE simulations can compute a continuous wave (CW) solution for the geometry, in addition to pulses and other time-variant waveforms. In the latter case, a pulse is defined at the transmitter (TX) in the time-domain, and is then decomposed into its spectrum via a Fourier Transform. For each frequency, the complex amplitude of the spectrum defines the source amplitude, from which the field is solved spatially. Receivers are defined at a discrete number of points in the ice, and the complex amplitude is sampled at these points for each frequency allowing the received pulsed to be re-synthesized via an inverse Fourier transform. The PE method has been shown to accurately replicate simulation results from Finite Difference Time Domain (FDTD) and ray tracing (RT) methods within ice geometries on a scale of several hundred meters [10]. At the same time, the greater simulation efficiency of PEs with respect to FDTD allows them to simulate much larger ice geometries ($O(\sim \text{km})$) than are feasible with FDTD simulations[10].

3. Propagation through glacial firn

Firn is the transitional stage between newly fallen snow and glacial ice. Over time, a layer of fallen snow is buried and compacted beneath new layers of accumulated snow. After breaking of the snow flakes by wind action and subsequent re-crystallization, aged surface snow has densities of $\sim 0.3\,\text{g/cm}^3$. Compaction and grain growth dominate the densification process until the firn density reaches $\rho \sim 0.55\,\text{g/cm}^3$, from which point the process is dominated by sintering. The density profile $\rho(z)$ of a 'cold glacier', and hence the $n(z)$ profile is described analytically via the relationships [11, 12]:

$$\rho(z) = \rho_{\text{ice}} + (\rho_s - \rho_{\text{ice}})e^{-kz} \quad \text{and} \quad n(z) = 1 + 0.845\rho(z). \tag{4}$$

With k being the densification rate factor, which itself is temperature and pressure dependent, as described by numerous models[11], including the Herron-Langwey (HL) model[13]. However real-world glaciers are subject to solar forcing from the sun exposure, which can cause melting of surface snow. The melt water percolates downwards through the firn and refreezes at some depth, forming anomalous ice layers with higher density[11]. Low density layers, called 'depth hoar' have also been observed [11], which form due to pyramidal or cup shaped crystals. Both the presence of high density ice layers and low density hoar will lead to significant internal reflections within the ice.

To illustrate the effects of density fluctuations on RF propagation, we show RF propagation within the the firn layer at the Summit station in Greenland, located at an altitude of 3217 metres above sea level. The $n(z)$ at this location has been estimated by measuring density of ice cores, neutron scattering and the inversion of ice penetrating radar[14]. The inversion of the radar data returns a best-fit profile $n_{HL}(z)$ defined by the HL-model [13]. However significant variation exists between the measured $n(z)$ using the density and ice-core methods and the best-fit model, with root-mean-squared values of density variance on the order of $\Delta\rho_{rms} \sim 18.0\,\text{kg/m}^3$ at $z = 1\,\text{m}$ to $\Delta\rho_{rms} \sim 8.0\,\text{kg/m}^3$. This results in uncertainty of the $n(z)$ with respect to depth of $\Delta n \sim 0.02$ to ~ 0.04. Here the scenario is explored that these residual errors reflect random density fluctuations with respect to depth, on the same scale of the residual errors. The resulting variance of the $n(z)$ is displayed in fig. 1. 60 $n(z)$ profiles are sampled $n_{rand}(z)$ with random fluctuations $\Delta n(z)$ added to the HL-model profile $n_{HL}(z)$. Each randomized profile is used to define a $n(z)$ model used for

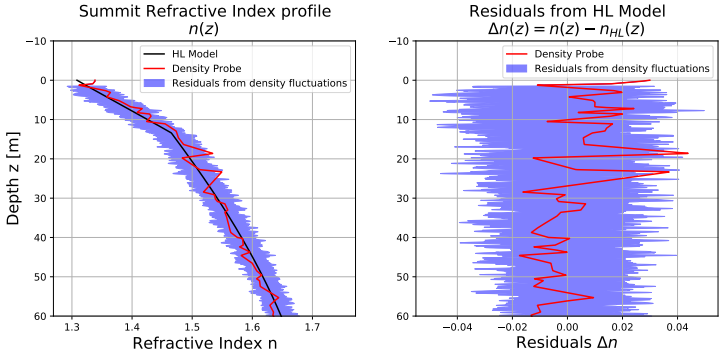

Figure 1: Estimates of the 1D $n(z)$ depth profile $n(z)$ of the Summit firn layer.

a paraProp simulation.

The transmitted signal is modeled as an impulse which has passed through a band-pass filter with a central frequency of $f_{centre} = 130\,\text{MHz}$ and the 3 dB threshold bandwidth of $B = 226\,\text{MHz}$ (Minimum frequency $f_{min} = 44\,\text{MHz}$ and maximum of $f_{max} = 270\,\text{MHz}$), with the source located at $z_{tx} = 8.0\,\text{m}$. The time-domain extends to $t_{max} = 600\,\text{ns}$ and has a resolution of $dt = 1\,\text{ns}$. The spectrum of the resulting pulse is used to define the transmission spectrum, in intervals of $\Delta f = 1.667\,\text{MHz}$ from $f = \Delta f$ to the Nyquist frequency $f = 500\,\text{MHz}$. The propagating signal is sampled at a set of receivers, located at a horizontal range of $R = 30\,\text{m}$, and depths from $z_{rx} = 0.0\,\text{m}$ to $z_{rx} = 28\,\text{m}$, in steps of $\Delta z = 2.0\,\text{m}$. This is done by averaging the obtained amplitudes of the position of the antenna (assumed to be 1 m in height) and folding in the effective height $h_{\text{eff}}$of the antenna, assumed to be equivalent to the RX antennas used in the RICE experiment [7].

The effect of density fluctuations on the received pulses can be seen clearly in figure 2, where the pulse received at $z_{rx} = z_{tx} = 8.0\,\text{m}$ is displayed. Here the pulse simulated through the ice defined with the HL model $n_{HL}(z)$ is compared with 3 pulses made from the randomized profiles $n_{rand}(z) = n_{HL}(z) + \Delta n(z)$. All of the pulses feature the first arriving pulse at $t = 192\,\text{ns}$ and a secondary reflected component arriving at $t \sim 210\,\text{ns}$. The arrival time of the first arriving pulse matches the expected arrival time for horizontal signal propagation given the refractive index at this depth $t = Rn(z = z_{tx})/c$. The amplitude of the first arriving pulses varies significantly between the 3 different examples, and the variation seen clearly in the pulses' spectra. A notable feature is that the change of the received signal amplitude is more pronounced at the higher frequency range of the spectrum $f \gtrsim 200\,\text{MHz}$, with amplitude gain $G(f) = A_{rand}(f)/A_{HL}(f)$ factors of $O(0.3)$ to $O(3)$, than for the lower frequency range. However the arrival times of the direct and reflected components of the signals are the same to within an error of $\Delta t = 5\,\text{ns}$, consistent with the pulse width.

In fig. 3 and the variation of the received amplitude and instantaneous phase is shown for the frequency at $f = 150\,\text{MHz}$, $z_{tx} = 8\,\text{m}$ and RX locations of $(30\,\text{m}, 2.0\,\text{m})$, $(30\,\text{m}, 4.0\,\text{m})$ and $(30\,\text{m}, 8.0\,\text{m})$. The variation is displayed in a histogram of the ratio of the signal amplitudes propagating through the fluctuation profiles to the signal propagation through the HL-defined ice. It can be seen that changes in the density, on the order of 2% that of the analytical model can produce amplitude changes of greater than 50% in paraProp for shallow receiver depths, and phase shifts on the order of 100°. The RF power as a function of space is displayed in fig. 4, comparing the

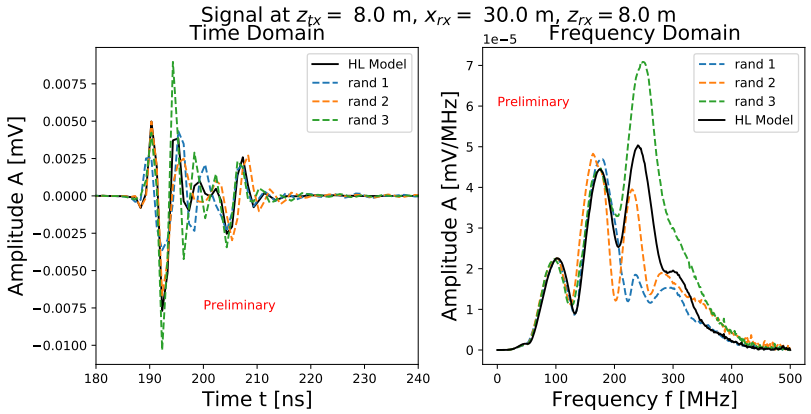

Figure 2: Left: the absolute amplitude of simulated pulses measured at $z_{rx} = 8.0\,\text{m}$ and $x_{rx} = 30\,\text{m}$ using the HL fit $n_{HL}(z)$, and 3 randomized profiles $n_{rand}(z)$. Right: the spectra of the received pulses.

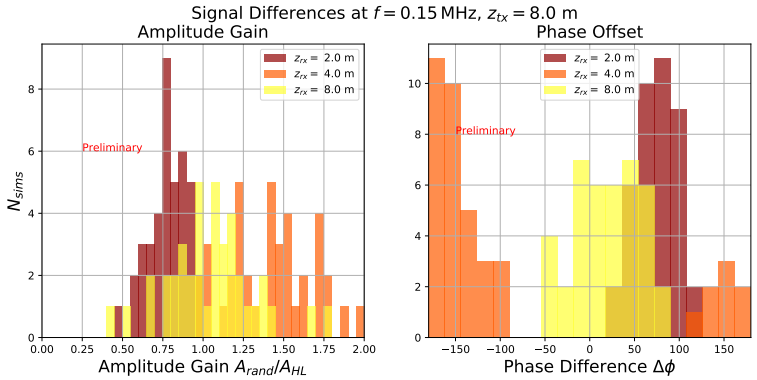

Figure 3: The variation of the amplitude (left) at $f = 150\,\text{MHz}$ between the HL model defined propagation and the density fluctuations. The variation of the instantaneous phase is shown on the right.

HL-model ice with a randomized firn model (fig 4a). as well as the ratio of the two models (fig. 4b). The interference fringes seen in the ice are shifted in space due to the density fluctuations, and the shift is frequency dependent, leading to modification of the frequency spectrum and hence the pulse shape. The output of paraProp simulations suggests that small scale density fluctuations have a significant and observable impact on signal propagation through glacial firn, and thus neutrino reconstruction studies will need to account for these effects.

4. Range dependent ice profiles

In previous radio neutrino propagation studies, the simulations have implicitly assumed range independence of the firn's $n(z)$ profile, varying only with depth. In reality polar firn will feature some surface roughness. The refractive index below the surface will also vary with range, with ice penetrating radar studies designating reflective layers as 'isochrones' and may mirror but not exactly match the surface topography. It is possible to model a changing surface elevation in paraProp by defining a 'digital elevation model' (DEM). This is accomplished by shifting the $n(z)$ values up or down by the same amount as the difference of the surface elevation from a flat surface. A primary goal of this work is to detect targets in ice via the back-scatter of a radar signal, and

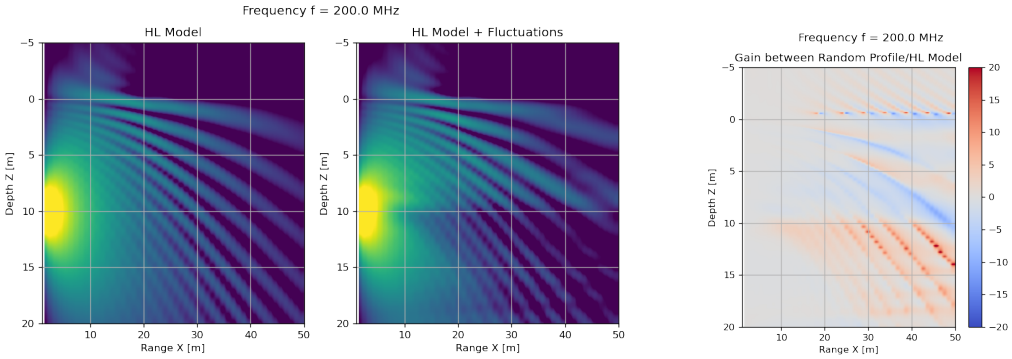

(a) **(b)**

Figure 4: An example of PE simulated CW propagation through Summit, with the Herron-Langwey (HL) model defined ice (left), and the HL model + density fluctuations (right)

to model how such a back-scatter is affected by the refractive index of the intervening ice. This can be done by solving the two-way parabolic equation, first for the forward-going wave from the origin to the maximum range of the domain, with the refractive index defined with a 2D matrix. An anomalous object, such as crevass, can be represented in this matrix. If changes in the $n(x, z)$ exists in the x-directions ($dn/dx > 0$), these distances are used to define reflective sources for the backwards propagating wave, with an amplitude defined with the field amplitude at the reflector's range multiplied by Fresnel's reflection coefficient.

5. Inversion of ice penetrating radar data with PEs

In addition to performing 'forward modelling' of RF propagation from a given $n(z)$ model, it is also possible to use PE simulations obtain a 'best fit' $n(z)$ model from a set of cross-borehole radar data $A_{data} = A_{data}(\hat{r}_{TX}, \hat{r}_{RX}, t)$, obtained by moving transmitting and receiving antennas across different depths within boreholes (such as in the diagram in fig 5b). This data inversion is done with the use of a genetic algorithm (GA) to 'evolve' a population of $n(z)$ models over a number of generations. A subset $n(z)$ values are represented as genes, with a granularity of $\Delta z = 0.5$ m and the remaining values interpolated. For each generation, the models are used to define the $n(z)$ of the ice domain, in which a pulse is emitted from the TX positions $\hat{r}_{tx}$ and received at the RX positions $\hat{r}_{rx}$. The similarity between the simulated data $A_{sim} = A_{sim}(\hat{r}_{TX}, \hat{r}_{RX}, t)$ and the real world data A_{data} using a fitness score S, which is evaluated as the sum of the fitness scores s for each TX and RX combination used in measurement.

$$S(n(z)) = \sum_{i}^{N_{TX}} \sum_{j}^{N_{RX}} s(A_{sim,i,j}(n(z)), A_{data,i,j}) \tag{5}$$

s may be evaluated using the inverse of the difference between the complex signal amplitudes of data and simulation. The fitness score S is used to select 'parents' from which the next generation of $n(z)$ models is generated. These are generated via cloning (a previous $n(z)$ model is copied to the next generation), mutation (one gene is replaced with a random number), and cross-breeding (the genes from two parents sampled to form a new individual). The process repeats until an optimal $n(z)$ profile is generated, which reconstructs the signal to within predefined residual error. The full

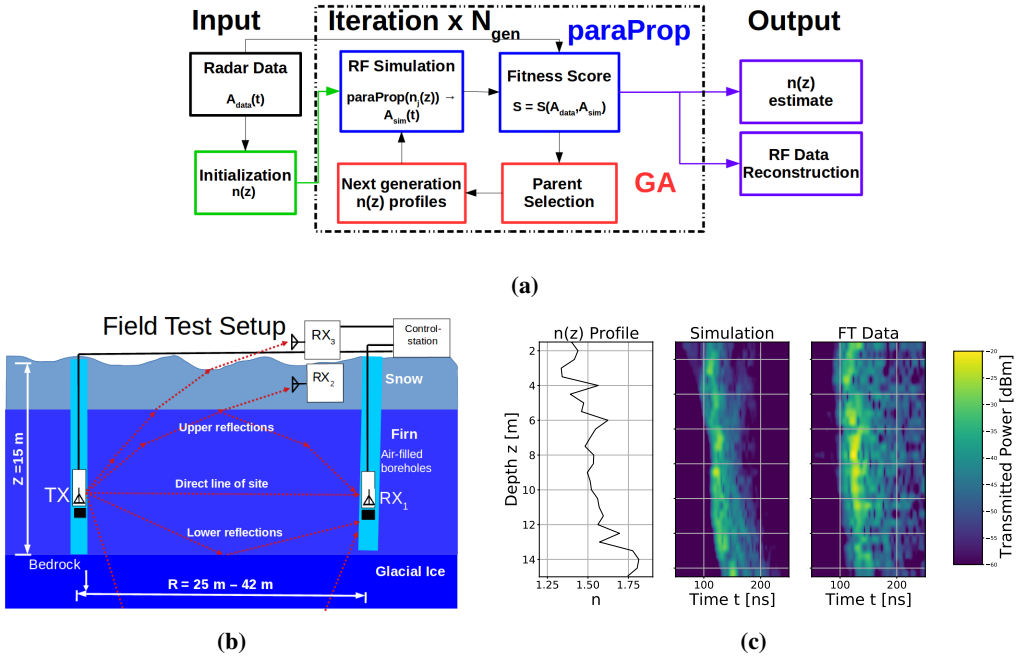

Figure 5: 5a The GA-based reconstruction-workflow with paraProp. 5b, the setup of a cross-borehole radar for measuring the $n(z)$ of ice. Example of $n(z)$ and RF signal reconstruction using GA-based inversion. A: displays the best-fit $n(z)$ profile, with B showing the RF power as a function of depth (where the TX and RX are at equal depths at a range of 25 m) for the simulation. C shows the obtained field test data for the equivalent measurement geometry

procedure is illustrated in fig. 5a. An ongoing analysis aims to reconstruct the $n(z)$ profile of the upper firn layer at the Aletsch glacier using cross-borehole radar, with preliminary reconstruction of the $n(z)$ profile and the signal data at different depths shown in fig. 5c. At present this inversion is able to reconstruct $n(z)$ profiles to an uncertainty $\Delta n < 0.05$ at all depths, not yet sufficient to accurately reconstruct the propagating signal amplitude.

6. Outlook

We have presented improvements to parabolic equation simulations of in-ice radio propagation, including the capability to model pulsed and continuous-wave emission through range dependent refractive index profiles which can be defined using existing density data. Using modelled and measured $n(z)$ of the upper Summit firn, PE simulations predict that relatively small scale density fluctuations in the firn layer can lead to significant discrepancies in the received signal amplitude from predictions derived from analytical approximations of the $n(z)$. These propagation effects result in systematic errors in the reconstruction of cascade energy and arrival direction. Future works will aim to quantify these systematic uncertainties. Finally, we have presented a method to estimate the $n(z)$ in-situ using a genetic algorithm based inversion of cross-borehole radar data.

References

[1] M. Aartsen, M. Ackermann, J. Adams, J. Aguilar, M. Ahlers, M. Ahrens et al., *The IceCube neutrino observatory: instrumentation and online systems*, *Journal of Instrumentation* **12** (2017) P03012.

[2] G.A. Askar'yan, *Excess negative charge of an electron-photon shower and its coherent radio emission*, *Zh. Eksp. Teor. Fiz.* **41** (1961) 616.

[3] P.W. Gorham, *On the possibility of radar echo detection of ultra-high energy cosmic ray- and neutrino-induced extensive air showers*, *Astroparticle Physics* **15** (2001) 177.

[4] S. Prohira, K. de Vries, P. Allison, J. Beatty, D. Besson, A. Connolly et al., *The radar echo telescope for cosmic rays: Pathfinder experiment for a next-generation neutrino observatory*, *Physical Review D* **104** (2021) .

[5] I. Plaisier, S. Bouma and A. Nelles, *Reconstructing the arrival direction of neutrinos in deep in-ice radio detectors*, *The European Physical Journal C* **83** (2023) .

[6] Ara Collaboration, P. Allison, J. Auffenberg, R. Bard, J.J. Beatty, D.Z. Besson et al., *Design and initial performance of the Askaryan Radio Array prototype EeV neutrino detector at the South Pole*, *Astroparticle Physics* **35** (2012) 457 [1105.2854].

[7] I. Kravchenko, G. Frichter, D. Seckel, G. Spiczak, J. Adams, S. Seunarine et al., *Performance and simulation of the RICE detector*, *Astroparticle Physics* **19** (2003) 15.

[8] A. Anker, S. Barwick, H. Bernhoff, D. Besson, N. Bingefors, D. Garcí a-Fernández et al., *Neutrino vertex reconstruction with in-ice radio detectors using surface reflections and implications for the neutrino energy resolution*, *Journal of Cosmology and Astroparticle Physics* **2019** (2019) 030.

[9] C. Deaconu, A.G. Vieregg, S.A. Wissel, J. Bowen, S. Chipman, A. Gupta et al., *Measurements and Modeling of Near-Surface Radio Propagation in Glacial Ice and Implications for Neutrino Experiments*, *Phys. Rev. D* **98** (2018) 043010 [1805.12576].

[10] S. Prohira, C. Sbrocco and A.P. et al, *Modeling in-ice radio propagation with parabolic equation methods*, *Physical Review D* **103** (2021) .

[11] C. Buizert and M. Helsen, *Firn*, in *Glaciers and Ice Sheets in the Climate System. Springer Textbooks in Earth Sciences, Geography and Environment*, A. Fowler and F. Ng, eds., pp. 255–277", Springer, Cham (2020), DOI.

[12] G.D.Q. Robin, *Velocity of radio waves in ice by means of a bore-hole interferometric technique*, *Journal of Glaciology* **15** (1975) 151–159.

[13] M.M. Herron and C.C. Langway, *Firn densification: An empirical model*, *Journal of Glaciology* **25** (1980) 373–385.

[14] R. Arthern, H. Corr, F. Gillet-Chaulet, R. Hawley and E. Morris, *Inversion for the density-depth profile of polar firn using a stepped-frequency radar*, *Journal of Geophysical Research: Earth Surface* **118** (2013) .

Full Authors List: The Radar Echo Telescope Collaboration

P. Allison[1], J. Beatty[1], D. Besson[2], A. Connolly[1], A. Cummings[3], C. Deaconu[4], S. De Kockere[5], K.D. de Vries[5], D. Frikken[1] C. Hast[6], E. Huesca Santiago[5], C.-Y. Kuo[7], A. Kyriacou[2] U.A. Latif[5], V. Lukic[5], K. Mulrey[8], J. Nam[7], K. Nivedita[8], A. Nozdrina[2], E. Oberla[4], S. Prohira[2], J.P. Ralston[2], M.F.H. Seikh[2], R.S. Stanley[5], S. Toscano[9], D. Van den Broeck[5], N. van Eijndhoven[5], and S. Wissel[3]

[1]Department of Physics, Center for Cosmology and AstroParticle Physics (CCAPP), The Ohio State University, Columbus, OH, USA

[2]University of Kansas, Lawrence, KS, USA

[3]Departments of Physics and Astronomy & Astrophysics, Institute for Gravitation and the Cosmos, Pennsylvania State University, University Park, PA, USA

[4]Astronomy & Astrophysics, Kavli Institute for Cosmological Physics, University of Chicago, Chicago, IL, USA

[5]Interuniversity Institute for High Energies, Vrije Universiteit Brussel, Brussel, Belgium

[6]SLAC National Accelerator Laboratory, Menlo Park, CA, USA

[7]National Taiwan University, Taipei, Taiwan

[8]Department of Astrophysics/IMAPP, Radboud University Nijmegen, P.O. Box 9010, 6500 GL Nijmegen, The Netherlands

[9]Interuniversity Institute for High Energies, Université Libre de Bruxelles, Brussels, Belgium

Acknowledgements

RET-CR is funded in part by the National Science Foundation under grant numbers 2012980, 2012989, and 2306424, and the Office of Polar Programs, the Flemish Foundation for Scientific Research FWO-G085820N, the EU-ropean Research Council under the European Union's Horizon 2020 research and innovation program (grant agreement No 805486), and the Belgian Funds for Scientific Research (FRS-FNRS). SP acknowledges support from the IceCube EPSCoR Initiative and the John D. and Catherine T. MacArthur Foundation.

We would like to acknowledge the support staff at Summit Station, Greenland for all their assistance in deploying RET-CR. Without them, RET-CR would have never reached the commissioning and data taking phase.

The cross-borehole radar data used for refractive index reconstruction analysis was obtained as part of the Enceladus Explorer (EnEx) project. EnEx is an initiative of the German Aerospace Centre (DLR) Space Administration, funded by Germany's Federal Ministry for Economy and Climate Protection (BMWK).